BUffet and Transition delay control investigated within European-Russian cooperation for improved FLIght performance

D3.19 Report on the experimental results on transition delay in the "Juju" TRIN1 wind tunnel by the VR DBD actuators based on wall-normal jets

Reference :	BUTERFLI_D3.19_UNOTT_31032016		
Author(s) :	Jung-Hoon Kim Maxime Forte Kwing-So Choi	Email:	Kwing-so.choi@nottingham.ac.uk
Lead Beneficiary:	UNOTT	*Dissemination level :*	CO
Date :	31 March 2016	*Last update :*	3 May 2017
Validated by the WP L :			
Validated by the Russian Coordinator :			
Validated by the European Coordinator :			
Signature of the European Coordinator :			

Update	Name	Version
31/03/2016	D3.19	1.00
13/04 2017	D3.19 update	2.00
03/05/2017	D3.19 update final	3.00

Control of crossflow instability with virtual roughness (VR) plasma actuators

1. Experimental Setup

Wind tunnel test campaigns were carried out to investigate into a possible transition delay using VR (virtual roughness) plasma actuators by controlling crossflow instability over a swept wing. These tests took place at ONERA Toulouse between 29 April and 9 December 2016. The ONERA-D airfoil with 0.35m chord length was set to 60° of sweep angle and at the angle of attack of -8°. The freestream velocity (U_∞) was kept at 70 m/s, corresponding to the Reynolds number of 1.6×10^6.

The specifications of the ring-type plasma actuators prepared are shown in Table 1, where the 'GA' actuator sheet was used for the 1st campaign, while the 'P1' actuator sheet was used for the 2nd and 3rd campaigns. All actuator sheets were made of a 0.15 mm thick Cirlex sheet. With the 'GA' actuator sheet, we were able to test different VR spacing (either 3.5, 4, 4.5 or 6 mm) without reattaching the actuators sheet, meanwhile the constant 3.5 mm VR spacing was provided by the 'P1' actuator sheets. The leftmost VR of 'P1' sheets is located 313 mm from the left (upstream) edge.

The electrodes of the 'GA' actuator sheet are shown in Fig. 1 (a) and (b), while those of the 'P1' actuator sheet are shown in Fig. 1 (c) and (d). On installation to the airfoil, four rows of actuator rings are located at x/c = 1.9%, 3.3%, 4.7% and 6.1%. With these actuator sheets, we can simply connect the power supply to each row of ring actuator to test plasma actuators at different chord wise location. The lower electrodes were designed so that only one row of VR actuators is connected at a time. High amplitudes of sinusoidal voltage were applied to the plasma actuator sheets by TREK power amplifier (model 30/20, ±30 kV, 20 mA peak). Here, the quoted voltages refer to the values from peak to 0 volt.

Table 1 Specifications of the actuator sheets prepared.

Name	Spanwise Spacing (wave length) mm	No. of Actuator Rows	Ring Diameter (mm)	Qty.	Cirlex Dielectric Sheet		Campaign on test
					Size mm x mm	Thickness mm	
G4	4	1	1	1	297 x 400 (W) x (L)	0.15	-
G6	6	1	1	1			
GA	3.5, 4, 4.5 and 6 (on one sheet)	4	1	3			1st
P0.5	3.5	4	0.5	2	590 X 297 (W) x (L)		-
P1	3.5	4	1	2			2nd , 3rd

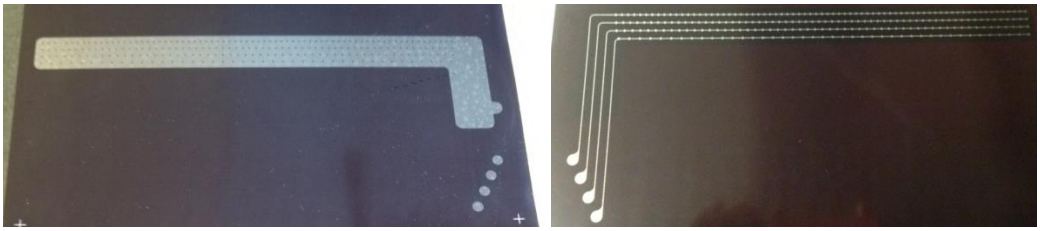

(a) (b)

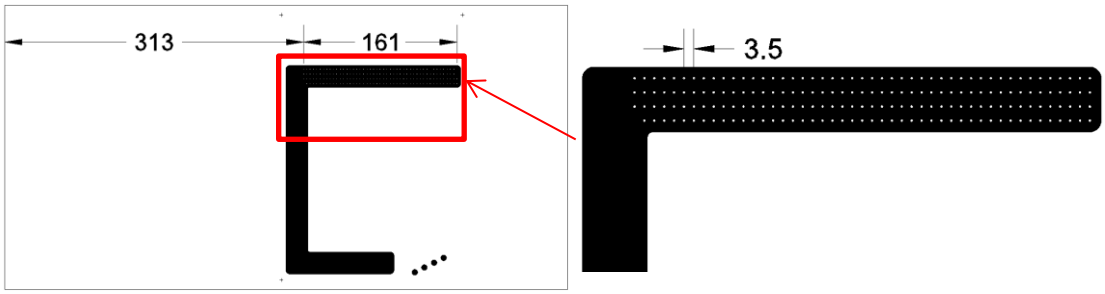

(c)

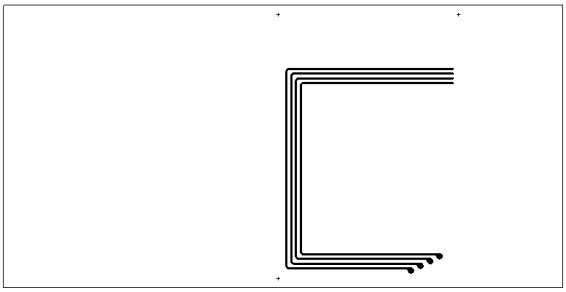

(d)

Figure 1 Photos of (a) the upper and (b) the lower (ground) surface in the 'GA' plasma actuator and drawings of (c) the upper and the magnified and (d) the lower (ground) surface of the 'P1' plasma actuator.

The actuator sheet was wrapped around from the pressure side of the airfoil at 50 mm from the leading edge, as shown in Fig. 2. During the 1st campaign, double-sided tapes were used only around the edges and the area directly beneath the upper electrodes. This resulted in small air bubbles, which we were not be able to get rid of. In the 2nd campaign, about 0.05 mm thick double-sided adhesive tape was used to cover the entire plasma actuator sheet. The air bubbles were, therefore, not present.

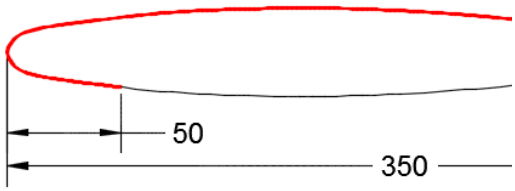

Figure 2 Cross-section of the ONERA D airfoil with the dielectric sheet (red line) mounted.

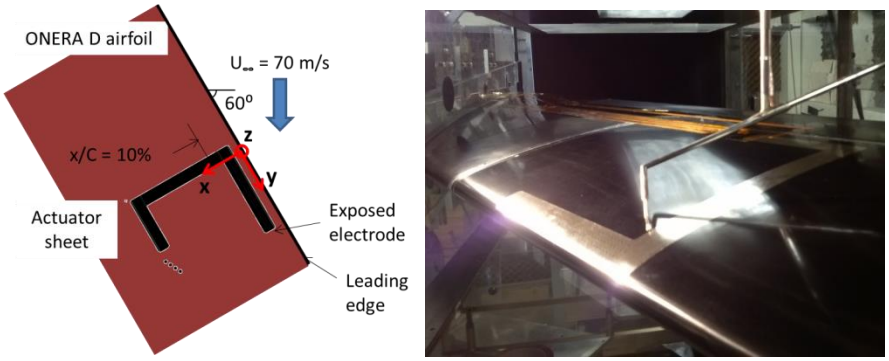

(a) (b)

Figure 3 Test set-up: (a) Plan view of schematic of the actuator sheet over the aerofoil and coordinates; (b) the photo of the airfoil with the actuator in the wind tunnel.

Schematic of the actuator sheet over the airfoil is given in Fig. 3. Here, x, y and z are chordwise, spanwise and vertical directions over the airfoil at zero angle of attack. Some hot-wire measurements were made in the freestream direction, which was later converted to the corresponding chordwise positions and expressed as a function of x. Fig. 4 shows the plasma glow discharge (in purple colour) from an array of VR actuators at 3.5 mm spacing.

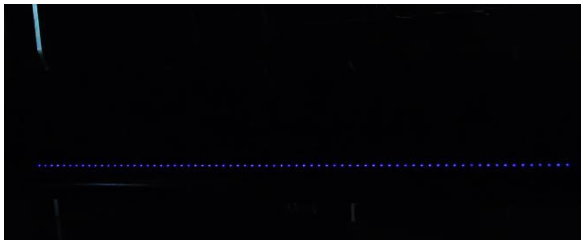

Figure 4 A photo of glow discharges from the actuator.

The hot-wire anemometry (Dantec Streamline, 90C10 CTA modules) with a hot-wire probe (Dantec 55P15) has been used in all flow measurements, as shown in Fig. 3 (b). The data sampling frequency was set at 20 kHz in the 1st and 2nd campaigns. It increased to 50 kHz in the 3rd campaign in an effort to capture the secondary instability signal predicted by DNS study by KTH team. During the 2nd and 3rd campaigns, the hot-wire probe was calibrated twice a day, once in the morning and the other in the afternoon outside the boundary layer at x/c = 20%. Here, the local inviscid velocities were obtained from C_p curves and the freestream velocities measured by Pitot tube at the inlet of the test section. The hot-wire calibration was carried out for the velocity between 20 m/s and about 75 m/s, which was fitted into King's law. The overheat ratio was set to be 0.8 and temperature corrections were made using the following formula,

$$E(T_0) = E(T)((T_h-T_0)/(T_h-T))^{0.5}$$

Where, T_0, T, T_h, E(T) and $E(T_0)$ are the flow temperature at hot-wire calibration, the flow temperature during the wind tunnel measurement, hot-wire operating temperature, the anemometer output voltage during the wind tunnel measurement, and the hot-wire output voltage E at hot-wire calibration. The data acquisition was made with 12 bit A/D converter. Here, the DC signals from the anemometer were used to obtain the mean velocity, while the band-passed AC signals (10 Hz to 8 kHz in the 1st and 2nd Campaigns and at 10 Hz to 20 kHz in the 3rd campaign) were used for fluctuating component. The amplifier gain was set to 10 on the AC signals.

2. Results

2.1 1st wind tunnel campaign

Plasma actuators with 3.5 mm spacing were investigated at x/c = 10%, representing the chord position closest to the leading edge. Spanwise distribution of RMS hot-wire voltage is shown in Fig. 5(a). Looking at the data when the DBD plasma actuator is OFF, there are some noticeable peaks but the RMS level is low and the wave form is not quite periodic. When the actuators are ON, the RMS amplitudes are nearly doubled and the wave form show small but clear 3.5 mm wavelength in some measurements, see Figs. 5(a) and 6(b).

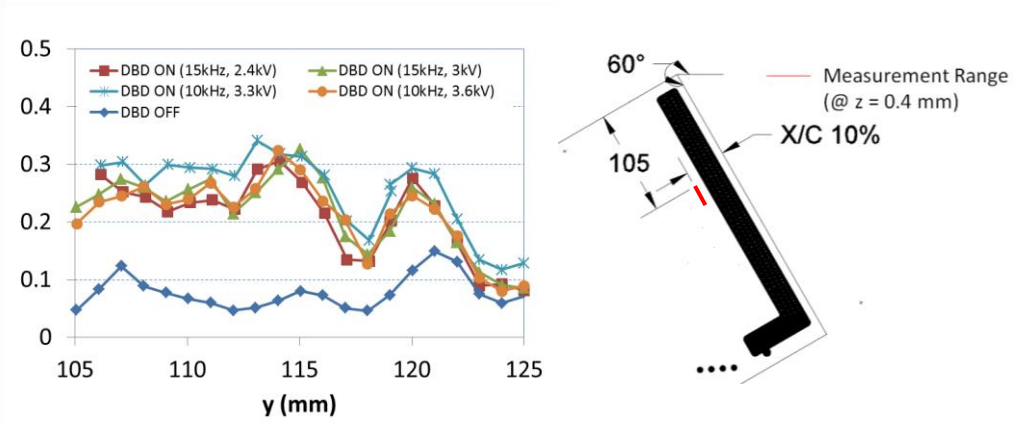

(a) (b)

Figure 5 (a) Spanwise distributions of RMS hot-wire voltage for the 3.5 mm-spacing actuators and (b) the measurement locations (x/c = 10%, 105 mm ≤ y ≤ 125 mm).

The effect of plasma actuators at this chord position (x/c = 10%) is similar even when different frequencies (10 KHz, 15 kHz and 23 KHz) and voltages (2.4 kV, 3.0 kV, 3.3 KV and 4.0 kV) are applied to the actuators, see Figs. 6(a) and 6(b). It seems that the effect of plasma actuation on the flow over the airfoil is not uniform along the span. Where the plasma actuation is effective, see Figs 5(a) and Fig. 6(b), the velocity fluctuation of the boundary layer is increased (as indicated by RMS voltages), where the waveform contains the spanwise wave length of the plasma actuators (λ = 3.5 mm). Where the plasma

actuation is not effective, see Fig. 6(a), there is no noticeable increase in the velocity fluctuation nor the wave form.

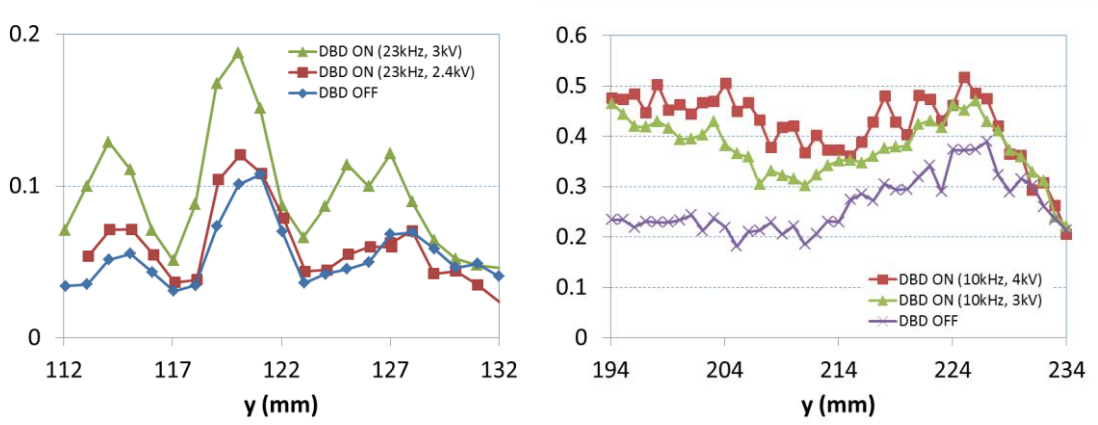

(a) (b)

Figure 6 Spanwise distributions of RMS hot-wire voltage for the 3.5 mm-spacing actuators at x/c = 10%; (a) between y = 112 and 132 mm; (b) between y = 194 and 234 mm.

Spanwise distributions of RMS hot-wire signals with plasma actuators with 3.5 mm spacing at further downstream location (x/c = 18%) are given in Fig. 7, showing that the wave form looks nearly identical with or without plasma actuation. It is also interesting to observe that the velocity fluctuation also remained at the same level, suggesting that the plasma actuators in this condition are not affecting the boundary layer transition at all. Here, the spanwise wavelength is about 6 mm, corresponding to the most dangerous wave length of cross-flow instability.

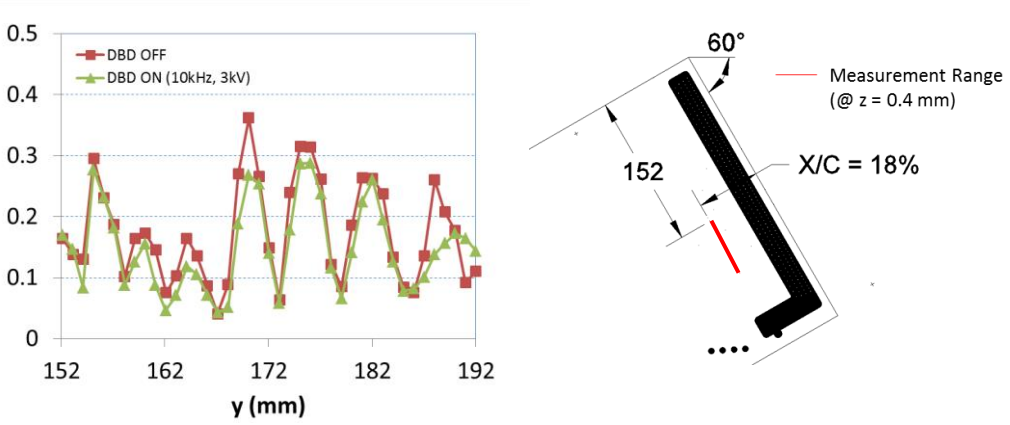

(a) (b)

Figure 7 (a) Spanwise distributions of RMS hot-wire voltage for the 3.5 mm-spacing actuators and (b) the measurement locations. (x/c = 18%, 152 mm ≤ y ≤ 192 mm).

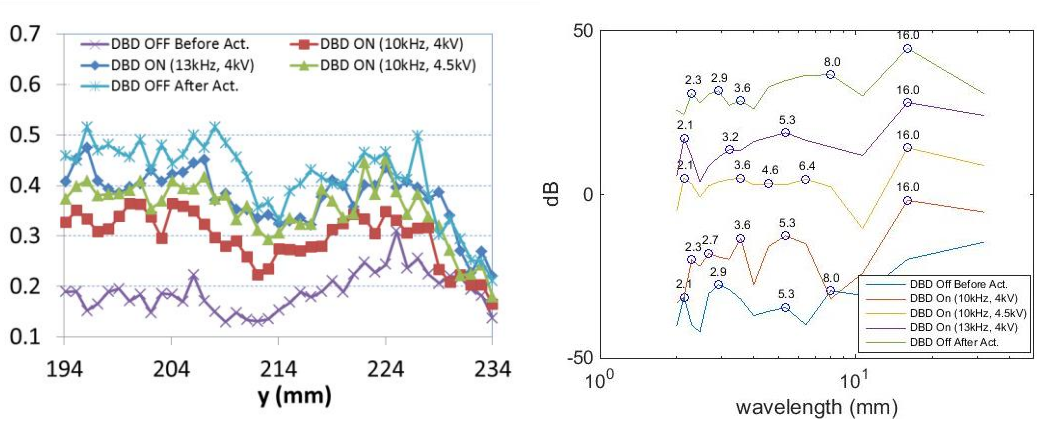

(a) (b)

Figure 8 (a) Spanwise distributions of RMS hot-wire voltage for the 4.5 mm-spacing actuators at x/c = 10% and 194 mm ≤ y ≤ 234 mm and (b) the corresponding power spectrum.

Next, the actuators with 4.5 mm spacing were investigated at x/c = 10%, where the spanwise measurements were made between y = 194 and 234 mm. The RMS voltage of hot-wire signals and their spatial power spectrum are shown in Fig. 8 (a) and (b), respectively. For the aim of distinction, a constant value (20 dB) was added to a profile compared to the one positioned lower in all the spectrums following. The horizontal axis of Fig. 8(b) is the spanwise wavelength. The numbers at each circles in Fig. 8 (b) indicates the wavelengths of the local peaks. Here, the amplitude around 6 mm wavelength component, which is known to be associated with the most unstable crossflow instability waves in our test conditions, appears to increase with an increase in the power supply to the plasma actuators. The results also suggest that the profiles for DBD OFF cases look quite different before and after the plasma actuations. After the actuation, for example, the broad peak around 6 mm appears to remain high. It is most likely due to a formation of local roughness created by erosion of the plasma electrode.

Fig. 9 shows the spanwise RMS hot-wire signals and the corresponding FFT analysis for the 4.5 mm-spacing plasma actuators. Here, the hot-wire measurements were made between y = 151 mm and 191 mm at x/c = 18% when the plasma sheet was actuated with 2.4 kV at 23 kHz. With the actuator on, the RMS values are seen to increase but the peak positions do not seem to change, see Fig. 9(a). On the other hand, the wavelength spectrum in Fig. 9(b) appears to indicate a broadening of 8 mm wavelength with the plasma actuator is ON.

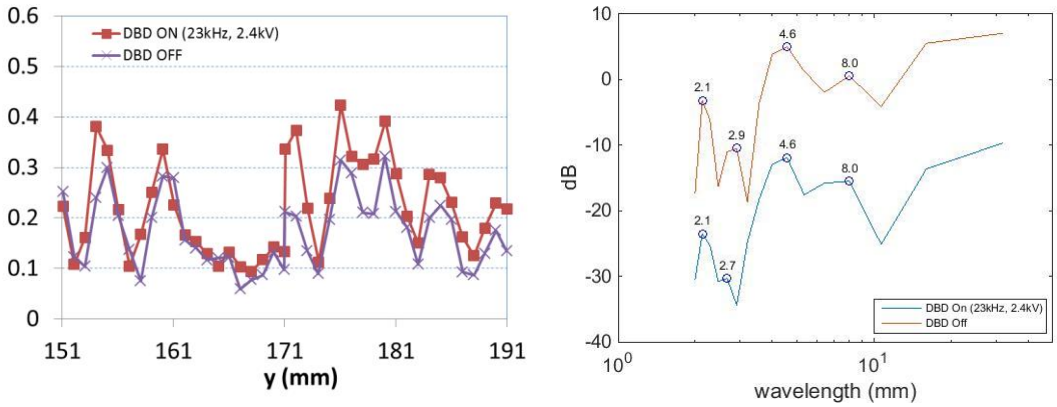

(a) (b)

Figure 9 (a) Spanwise distributions of RMS hot-wire voltage for the 4.5 mm-spacing actuators at x/c = 18% and 151 mm ≤ y ≤ 191 mm and (b) the corresponding power spectrum.

The spanwise RMS hot-wire signals and the corresponding FFT analysis for the 6-mm spacing plasma actuators are shown in Fig. 10 (a) and (b). As mentioned before, a constant value (10 dB here) is added to the upper profile with respect to the lower. Here, almost identical spacing of peaks can be seen in Fig. 10 (a) with and without plasma actuations. It can be seen from Fig. 8 (b) that the dominant wavelength is around 6 mm in both cases. This was the first test carried out after the actuator sheet was installed, therefore there should be no roughness effect due to the erosion of plasma electrode.

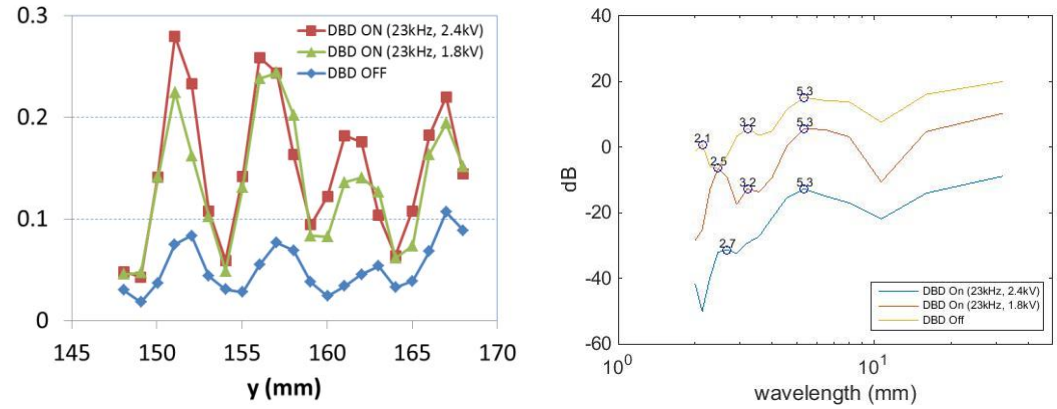

(a) (b)

Figure 10 (a) Spanwise distributions of RMS hot-wire voltage for the 6 mm-spacing actuators at x/c = 18% and 148 mm ≤ y ≤ 168 mm and (b) the corresponding power spectrum.

The chordwise distributions of RMS hot-wire signals are shown in Figures 11 (a) and 11(b) for the 3.5-mm and 6-mm spacing actuators, respectively, to demonstrate if the plasma actuators promote or delay the transition on the airfoil. These measurements were made in the streamwise measurement direction, from which the corresponding chord positions were obtained.

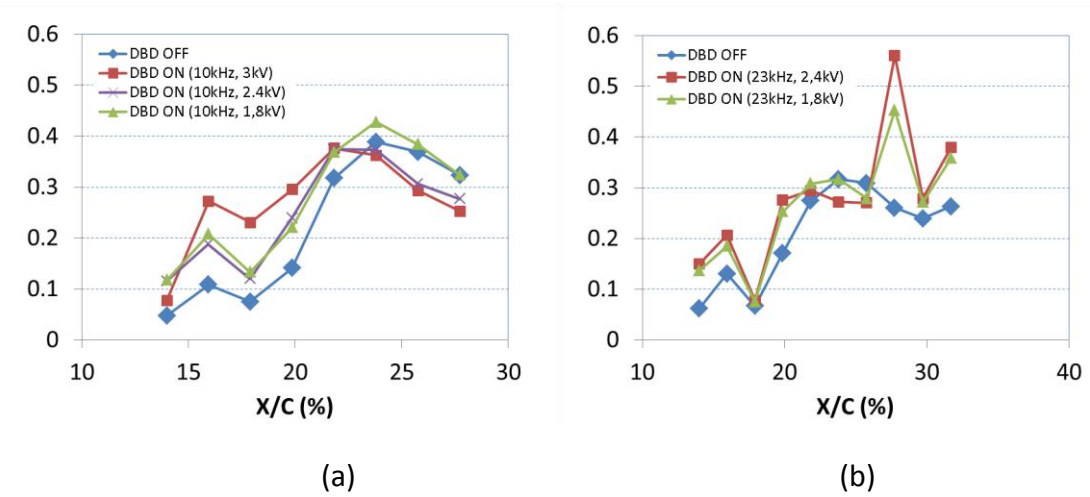

(a) (b)

Figure 11 Chordwise distributions of RMS hot-wire voltage: (a) the 3.5-mm spacing actuators; (b) the 6-mm spacing actuators.

Without actuation, the RMS hot-wire voltage increases sharply at around x/c = 18%, reaching the maximum value at x/c = 24%, suggesting that the transition to turbulence is taking place at this chord location. The RMS value decreases gradually afterwards. The time signals observed with the oscilloscope also indicated that the high-frequency fluctuations are increased as the hot-wire sensor was moved downstream. Beyond the chordwise position of x/c = 24%, the whole hot-wire signals were seen to fluctuate at high frequencies that the flow was thought to become turbulent, confirming the results shown in Fig. 11(a). The RMS levels are seen to increase when the actuator is on by shifting the RMS peak location upstream by x/c = 4%. A similar behaviour is seen in Fig. 11(b) with the 6-mm spacing actuators.

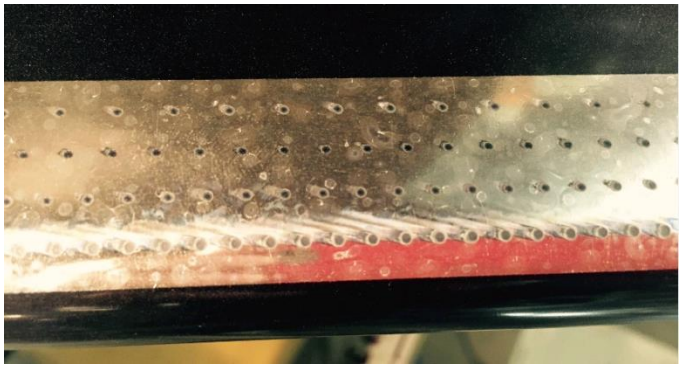

Figure 12 Stains left on the actuator sheet after wind tunnel tests.

After all the tests were completed, a photograph was taken of the exposed electrode, which is shown in Fig. 12. Around the ring edges, tail-like stains can be seen at the sweep angle of the airfoil. Possibly, the electrodes could have been oxidised by plasma being generated.

2.2 2nd wind tunnel campaign

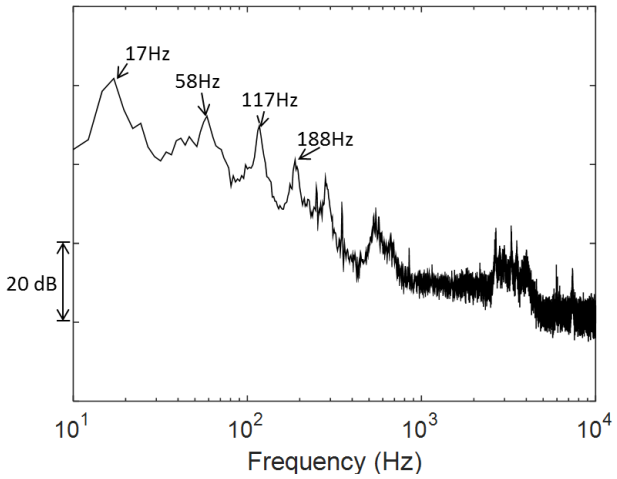

Figure 13 Power spectrum of velocity fluctuations measured at z = 0.4 mm and x/c = 20%.

In order to investigate the effects of VR plasma actuators with 3.5 mm spacing provided by the 'P1' actuator sheets, the RMS hot-wire signals were obtained in the boundary layer along the freestream direction at a constant height (z = 0.4 mm) over the airfoil. We can observe a number of peaks in the power spectrum, see Fig. 13, particularly in the low frequency range such as 17 Hz and 58 Hz and its harmonics (117 Hz and 188 Hz),. They are thought to come from the vibration of the hot-wire probe and its support in the boundary layer during the tests.

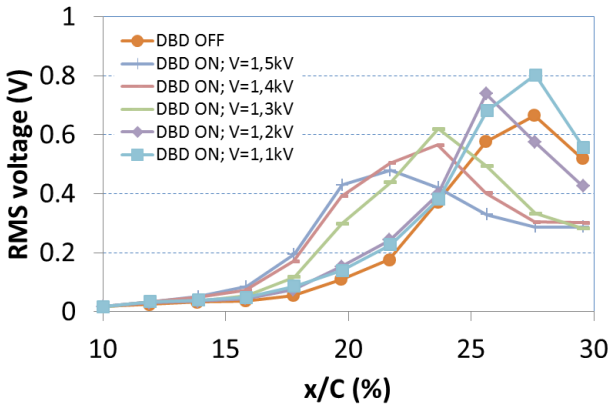

Figure 14 Streamwise developments of RMS of the hot wire signals high-pass filtered over 200 Hz at z = 0.4 mm.

Fig. 14 shows the developments of the RMS hot-wire voltages along the streamwise direction with and without plasma actuation. Here, these RMS values were obtained by integrating the fluctuating signals between 200 Hz and 10 kHz in the power spectra, removing the possible effect of probe/support vibrations. The supplied voltage to the actuators varied between $V_{p\text{-}0}$ = 1.1 kV and 1.5 kV (peak to 0), where the input frequency was fixed at 15 kHz. It is clearly seen from this figure that the transition points, represented by the RMS peaks, were shifted upstream by plasma forcing at the voltage input over 1.3 kV.

The power spectra of u-component velocity fluctuations corresponding to the data shown in Fig. 14 are given in Fig. 15. Here, the power spectra measured at the same chordwise locations are plotted at the same reference level. The power spectra at X/C = 10% appear to have no big difference with or without plasma forcing. However, the vertical position of the probe was not low enough to detect different signals at this chordwise location. At x/c = 12%, the spectral amplitudes are seen to increase between 2.5 kHz and 5.5 kHz for $V_{p\text{-}0}$ = 1.3, 1.4 and 1.5 kV. The spectral amplitudes at these frequencies increased further downstream at all test conditions. The power spectrum with plasma forcing at $V_{p\text{-}0}$ = 1.5kV becomes saturated at about x/c = 22%, which levels off in downstream. The spectral saturations with plasma forcing at lower voltages take places further downstream. The spectral saturation positions in Fig. 15 correspond to the RMS peak positions in Fig. 14. Other spectral humps in Fig. 15, such as those between 6 kHz and 8 kHz, seem to be due to the secondary instabilities. More discussions on these spectral humps will be given later.

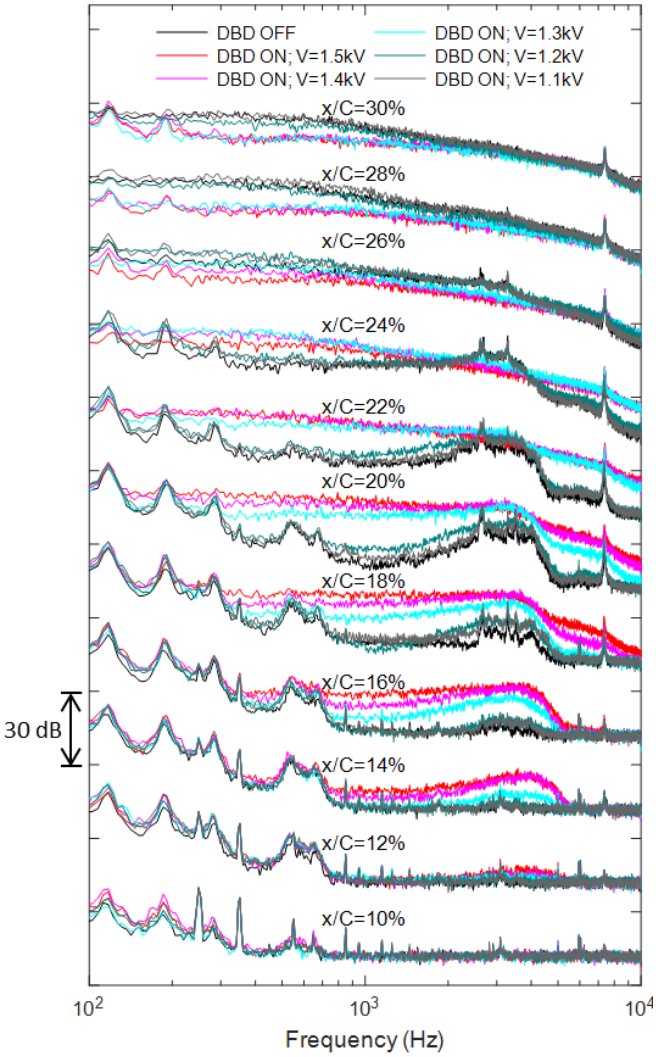

Figure 15 Power spectra of velocity fluctuations corresponding to the data in Fig. 14. The spectra at the same location of x/c are plotted with the same reference level.

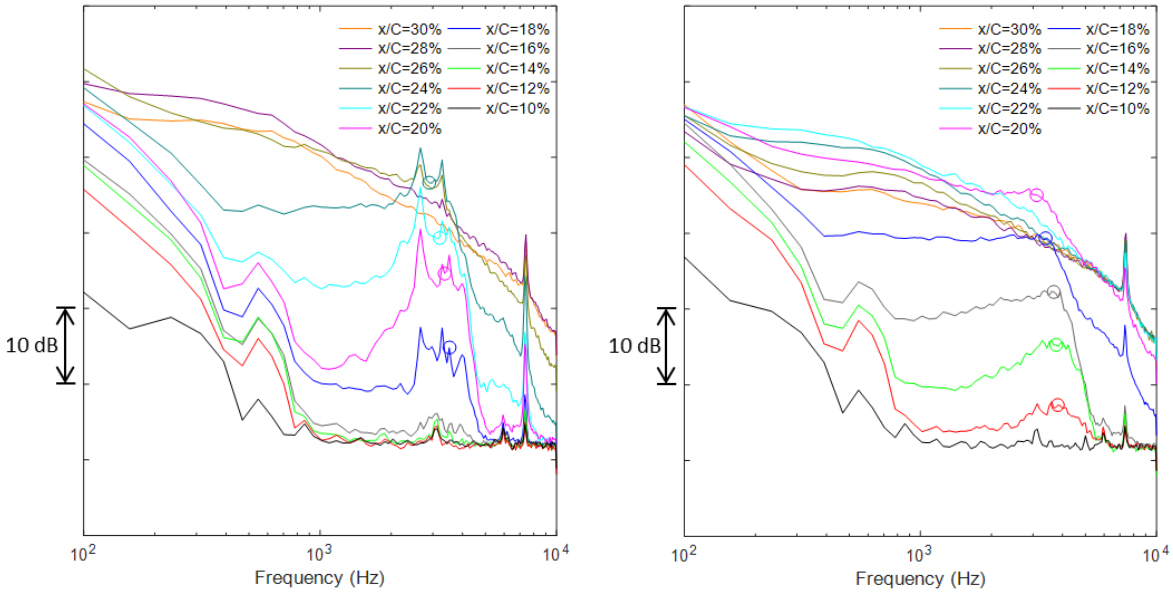

Figure 16 Power spectra of velocity fluctuations at various streamwise positions with (a) the actuator off and (b) with the actuator on with $V_{p\text{-}0}$ = 1.5 kV.

Figures 16(a) and 16(b) show the power spectra at different chordwise locations without and with plasma actuation at $V_{p\text{-}0}$ = 1.5 kV, respectively. Here, we have increased the amount of data in FFT to give better resolution in the spectra, particularly at higher frequencies. The broad peak frequencies are marked with 'o' symbols, at 2900 Hz, 3210 Hz, 3370 Hz and 3520 Hz without plasma forcing, see Fig. 16(a), and at 3100 Hz, 3400 Hz, 3670 Hz, 3770 Hz and 3820 Hz with plasma forcing, Fig. 16(b).

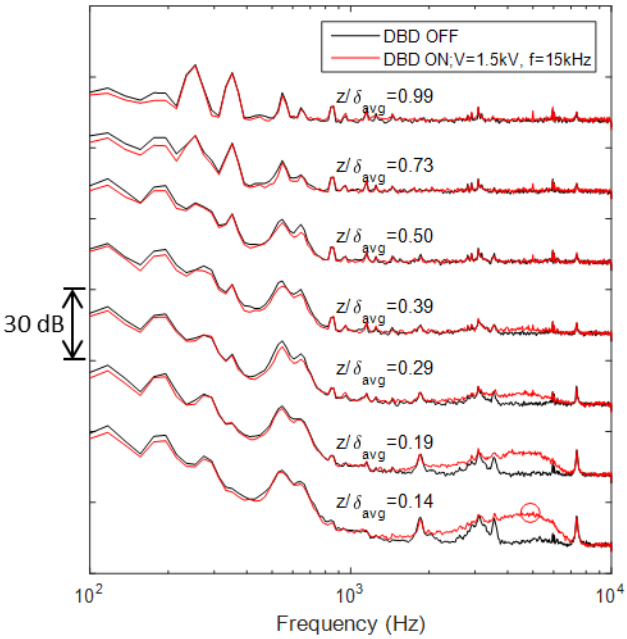

Figure 17 Power spectra of velocity fluctuations in the boundary layer at x/c = 10%. The reference levels are equal at the same z/δ_{avg}.

Fig. 17 compares the spectra at different wall-normal distance at x/c = 10 with plasma forcing at $V_{p\text{-}0}$ = 1.5 kV and frequency 15 kHz and without. Here, the wall-normal coordinate z is non-dimensionalised by the average boundary layer thickness, δ_{avg} = 0.37 mm. With plasma forcing, broad peaks at 4.9 kHz are seen below z/δ_{avg} = 0.39, marked by 'o', which indicates the frequency of growing instability waves.

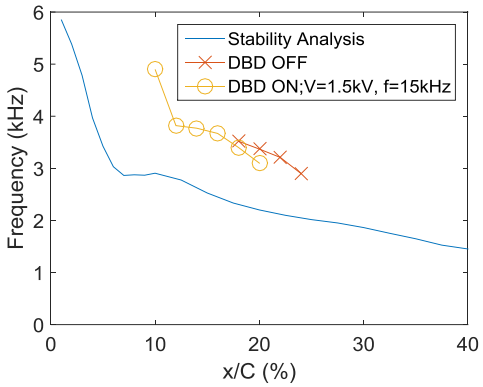

Figure 18 Distribution of the frequencies with maximum N factor in chordwise direction and measured broad peak frequencies.

In Fig. 18, the frequencies of broad peaks shown in Fig. 17 are compared with the predicted frequencies of maximum growth of instability (the N factor) obtained by DLR, showing a good agreement between the experiment and numerical analysis.

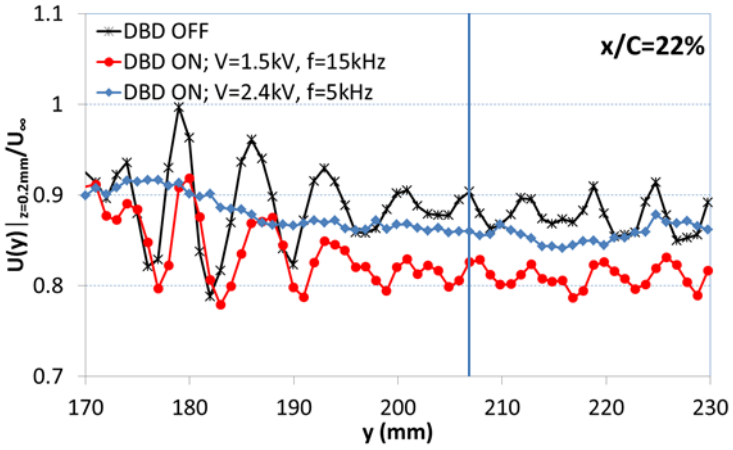

Figure 19 Spanwise distributions of the time-averaged velocities divided by U_∞ at z = 0.2 mm and x/c = 22%. The blue line is at y = 207 mm.

Fig. 19 shows the spanwise distributions of non-dimensional velocities in the boundary layer very close to the wall (z = 0.2 mm) at x/c = 22%, with and without plasma forcing. Due to the saturation of high voltage power supply, the increase in voltage applied to the plasma actuators was only possible with a reduction of frequency. These velocity profiles reveal the dominance of 6 mm wavelength, corresponding to that of most unstable stationary waves. However, such wavelength is absent when the supplied power was increased to $V_{p\text{-}0}$ = 2.4 kV. Corresponding non-dimensional velocity and turbulence intensity profiles at y = 207 mm

(see Fig. 19) are shown in Figs. 20(a) and 20(b), respectively. Here, the external velocity U_e just outside the boundary layer at the chordwise location is used for non-dimensionalise both the mean velocity and turbulence intensity, where $U_e = 0.94\ U_\infty$ at x/c = 22%. The shape factor was reduced from 1.70 to 1.53 with plasma forcing, confirming that the transition to turbulence is accelerated by the actuation. When the voltage applied to the plasma actuators is increased from 1.5 kV (red symbols) to 2.4 kV (blue symbols), the shape factor is further reduced to 1.31, indicating the completion of the laminar-to-turbulence transition.

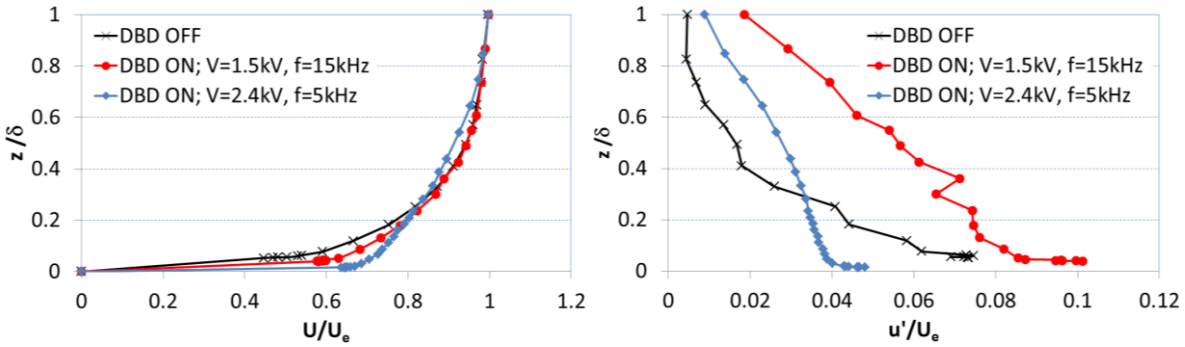

Figure 20 Boundary layer profiles measured at y = 207 mm and x/c = 22%: (a) Velocities; (b) Turbulence intensities. Both the quantities are non-dimensionalised by the external velocity outside the boundary layer at x/c = 22%.

The power spectra of velocity fluctuations in the boundary layer $z/\delta = 0.12$ at this position (y = 207 mm) are shown in Fig. 21, where a broad peaks at around 3150 Hz and 6300 Hz are observed without plasma forcing. Considering the boundary layer profiles and the power spectra as shown in Fig. 20 and Fig. 21, respectively, the disappearance of 6 mm wavelength that corresponds to that of most unstable stationary waves (see Fig. 19) is due to the completion of laminar to turbulent transition by plasma forcing at a higher voltage of V = 2.4kV .

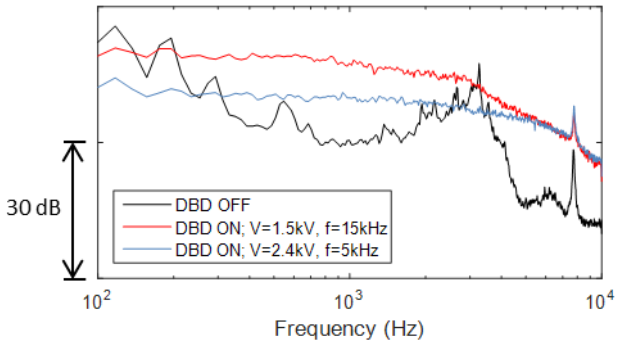

Figure 21 Power spectra of the velocity fluctuations at x/c = 22%, y = 207 mm and $z/\delta = 0.12$.

2.2 3rd wind tunnel campaign

In the 3rd and the final wind tunnel campaign we used the same 'P1' actuator sheet that was tested in the 2nd campaign. The frequencies of the secondary instability is predicted by KTH group to be about 14 kHz [3], therefore the sampling frequency of hot-wire signals was increased to 50 kHz in this campaign. This gave the power spectra of velocity fluctuations up to 25 kHz. We have also carried out detailed velocity profile measurements to investigate the spanwise variations associated with the secondary instability.

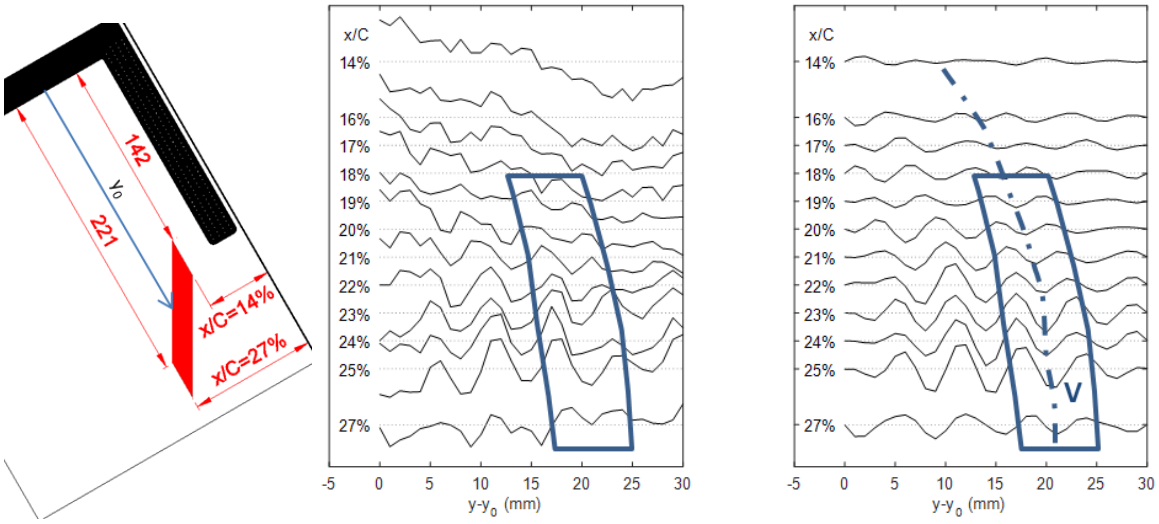

(a) (b) (c)

Figure 22 (a) Schematic for the measurement area (red) in plan view. y_0 is y values of the left edge of the measurement range at certain x/c, (b) Spanwise distributions of time-averaged velocities divided by the freestream velocity at z = 0.2 mm; (c) zero-phase shift filtered profiles in (b) with wavenumber band between 0.1/mm and 0.25/mm. The scales in (b) and (c) are arbitrary.

Figure 22(b) shows the spanwise velocity profiles close to the aerofoil surface (z = 0.2 mm) between x/c = 14% and 27% without plasma actuation. Here, y_0 is the location of each spanwise measurement, which varied between y_0 = 142 mm and 221 mm for x/c = 14% and 27%, see Fig. 22(a). The blue rectangles indicate the region of further hot-wire measurements in y-z planes to trace the development of the crossflow instability wave. By digitally bandpass filtering these spanwise velocity profiles, the development of most unstable crossflow instability wave with 6 mm wavelength can be clearly seen in Fig. 22 (c). The blue dash-dotted line designated represents the locations of lowest speed where the boundary layer is thickest.

Power spectra of the hot-wire signals along this blue dash-dotted line is given in Fig. 23, which does not show any significant differences across the 4-mm span. Here, v±1, v±2 symbols in the figure indicate the spanwise locations that are shifted by ±1 and ±2 mm from position v. The peaks just over 10 kHz are thought to be the elctrical noise [5], as they are also seen outside the boundary layer. This will be discussed later in Fig. 26.

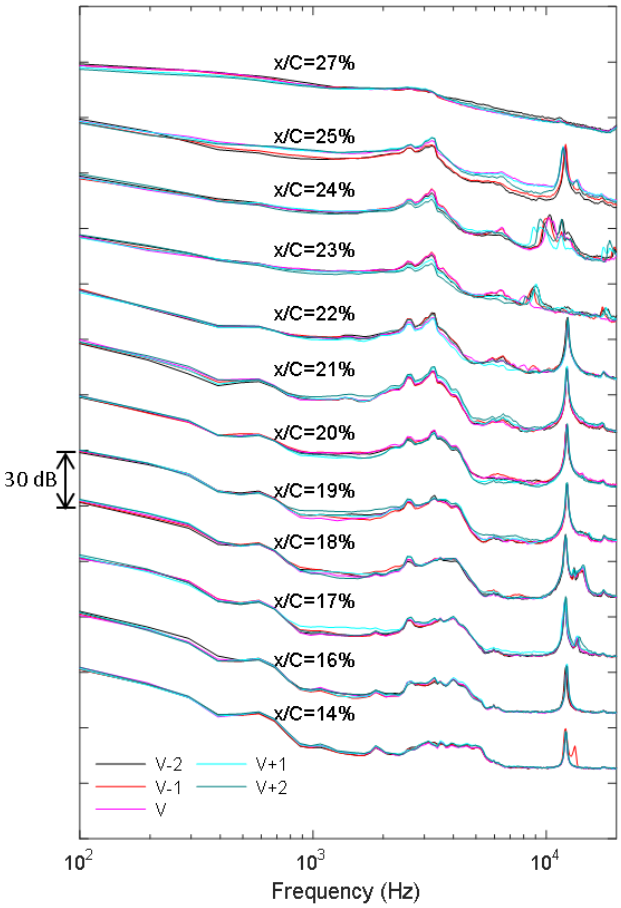

Figure 23 Power spectra of velocity fluctuations on 4 mm wide regions in spanwise direction along 'V' in Fig. 22 (c). The spectra at the same location of x/c are plotted with the same reference level.

More detailed hot-wire measurements without plasma actuations were made on the y-z planes in the blue rectangle region in Fig. 22 (c). Figure 24 shows the streamwise velocity contours, velocity and turbulence intensity profiles at each chordwise position, x/c = 21 to 27%. The measurements were taken at a 1 mm spanwise step along y-axis, where the hot-wire signals were band-pass filtered at 0.2 kHz and 10 kHz. Looking at the results shown in Fig. 14 and Fig. 16 (a), the last stage of transition to turbulence takes place at around x/c = 27%. However, the time-averaged velocity contours, Fig. 24 (a), do not show distortions as we expect from the saturation of the stationary waves [5]. Indeed, the velocity profiles, Fig. 24 (b), do not show the distinct S-shaped profiles, either. We suspect, therefore, that the transition to turbulence in our experiment could have taken place by the travelling crossflow waves at the same time as the stationary crossflow waves saturated. The turbulence intensity profiles at x/c = 27%, see Fig. 24(c), shows the development of peaks close to the wall, similar to that of fully developed turbulent boundary layer at this chordwise location.

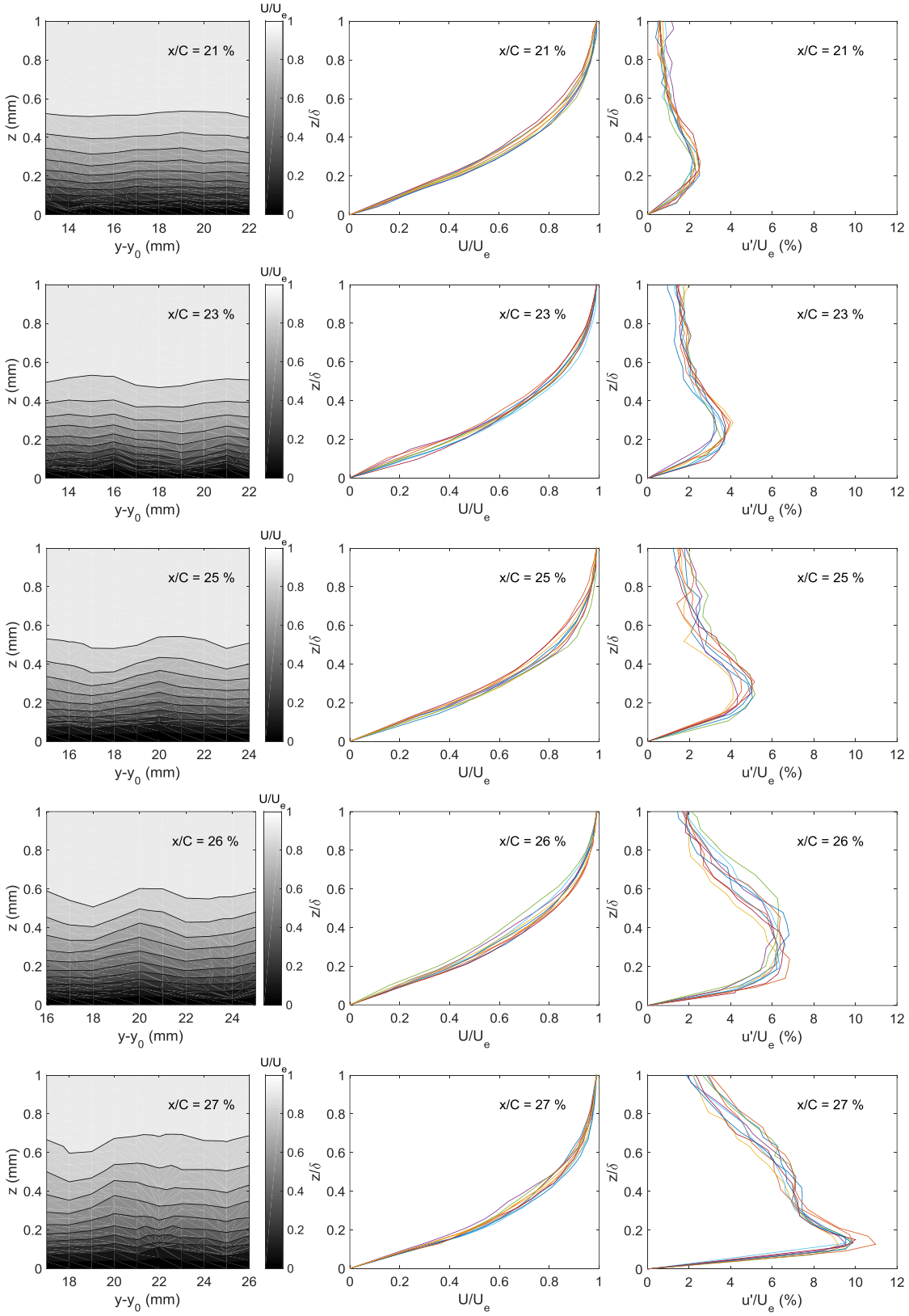

(a) (b) (c)

Figure 24 (a) Time-averaged streamwise velocity contours in the boundary layer, (b) time-averaged streamwise velocity profiles and (c) time-averaged boundary-layer instability modes filtered between 0.2 kHz and 10 kHz profiles at each chordwise location without actuation.

Figures 25(a), 25(b) and 25(c) show the velocity contours, velocity and turbulence intensity profiles, respectively, without and with plasma forcing ($V_{p\text{-}0}$ = 1.8 kV and f = 10 kHz) at x/c = 19%. For this test, the plasma forcing frequency was reduced from 15 kHz to 10 kHz to avoid the frequency (14 kHz) of predicted secondary instability wave [3]. At the same time, the voltage was increased from 1.5 kV to 1.8 kV to keep the power comparable to the previous case ($V_{p\text{-}0}$=1.5 kV and f = 15 kHz). These results indicate that the effect of plasma forcing on the boundary layer transition at x/c = 19% is very similar to the one at x/c = 27% without forcing.

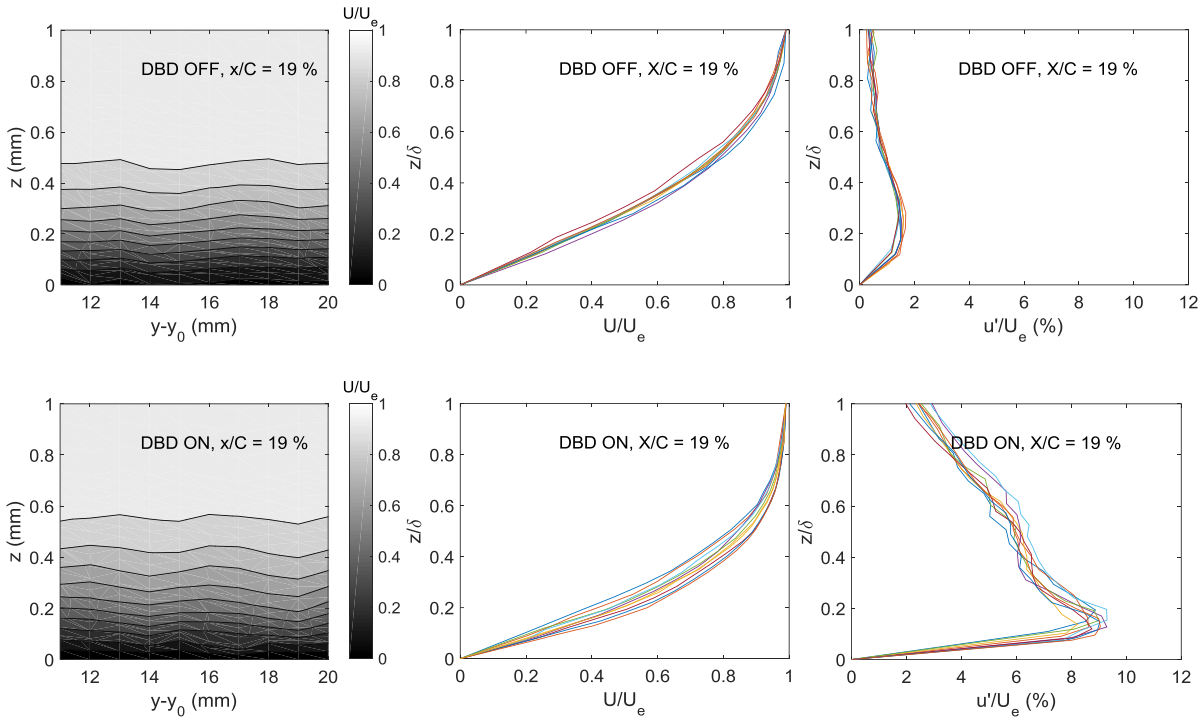

Figure 25 (a) Time-averaged streamwise velocity contours in the boundary layer, (b) time-averaged streamwise velocity profiles and (c) time-averaged boundary-layer instability modes. DBD OFF (upper) and DBD ON (lower) at $V_{p\text{-}0}$ = 1.8 kV and f = 10 kHz.

Fig. 26 shows the corresponding power spectra at different wall-normal positions. At this chordwise position (x/c = 19%) the laminar to turbulence transition is nearly complete with plasma forcing. Therefore, the spectral shape (shown in RED) does not seem to change across the boundary layer except that the high-frequency energy is increased with an increase in z. Without forcing (shown in BLACK), however, there are some significant differences in the spectral shape at different wall-normal position, such as the increase in the broadband level between 500 Hz and 2000 Hz near the edge of the boundary layer. As transition is still in progress without plasma forcing at this chordwise position, non-uniform development of disturbances in spanwise direction may result in these changes. The frequency peaks just above 10 kHz seem to be the electronic noise, since they are present even far away from the edge of the boundary layer.

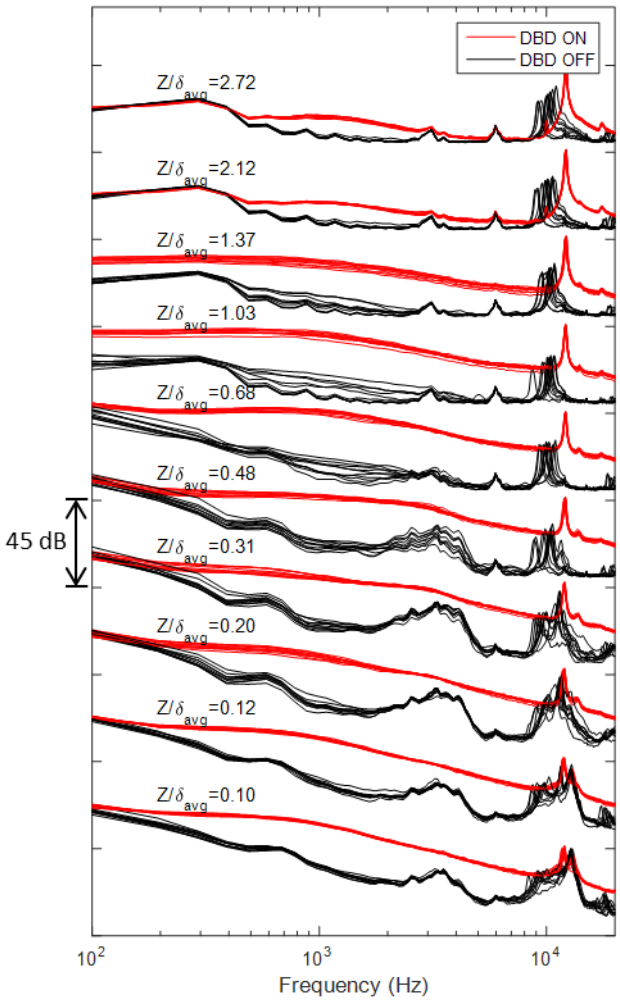

Figure 26 Collections of power spectra along the spanwise direction in the boundary layer at x/c = 19% with and without actuation ($V_{p\text{-}0}$=1.8 kV and f = 10 kHz). δ_{avg} = 0.82 mm which is mean of spanwise averages for both the cases.

Spanwise hot-wire measurements were made over a 30-mm distance at a 1-mm step, where the mean velocity was obtained at a constant height of z = 0.2 mm between x/c = 10% and 17%. Since the 3rd row of the actuators (located at x/c = 4.7%) were damaged in the previous tests, the 2nd row of actuators positioned at x/c = 3.3% were used instead for this test. Fig. 27 (a) shows the measurement area (shown in RED) for the present measurement, which was shifted slightly from the previous measurement area (shown in GRAY) to avoid the possible influence of the damaged actuators. Fig. 27 (b) shows the velocity power spectra as a function of the spanwise distance to indicate the wave length of the Fourier component with and without plasma actuation. Note that the power density in the y-axis is given in linear scale in this figure. All power spectra (with and without plasma forcing) in Fig. 27(b) seem to show a dominant peak at the wavelength $\lambda \approx 3$ mm throughout the chordwise measurements, although an increase in the power density at greater wavelengths is evident in the downstream. We suspect that these peaks at wavelength $\lambda \approx 3$ mm are the result of oxidised stains created at and around the plasma actuators after long operations, which acted as passive roughness with 3.5 mm wavelength.

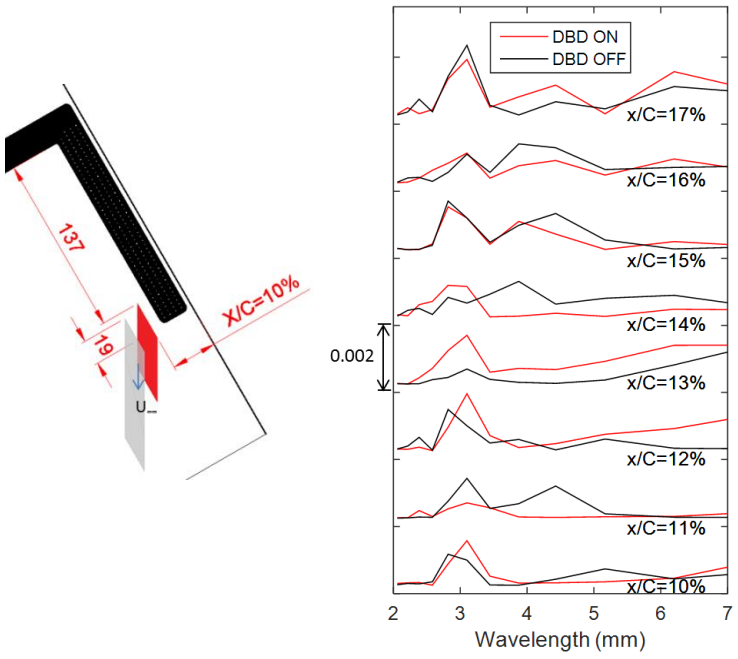

(a) (b)

Figure 27 (a) Measurement area for the present (red) and previous (grey) measurements in a plan view and (b) power spectra of the spanwise wavelength at z = 0.2 mm.

Conclusions

Crossflow instability control of the boundary layer over a swept ONERA-D airfoil was carried out using the virtual roughness (VR) based on an array of plasma actuators. Ring-type plasma actuators of various diameters, spanwise spacing and chord locations were operated at different forcing conditions in this investigation, which took place in TRIN1 wind tunnel at ONERA Toulouse. Careful hot-wire measurements were carried out in a wind tunnel to investigate if the virtual roughness could delay transition to turbulence when the crossflow instability is the primary route for transition to turbulence. As shown in Fig. 8 (a), some of the wind tunnel results in the first test campaign show that the VR promoted the crossflow instability wave of the same spanwise spacing, although the transition delay by the VR was not observed. Instead, the transition to turbulence was promoted by the VR in most test cases. These findings were confirmed by the measurements of mean velocity and turbulence intensity profiles as well as the time series of velocity fluctuations in the second and third test campaigns. Here, the energy spectra of velocity fluctuations showed the broad spectral peaks at around 3 kHz, whose downstream development was promoted by plasma forcing. We could not see clear indications of the secondary instability in any of the measurements, therefore we can conclude that the travelling waves would be interacting with the stationary waves in the transition process. This may explain why the VR was not successful in controlling the crossflow instability over a swept airfoil.

References

[1] J. Ray Dagenhart, Crossflow Stability and Transition Experiments In A Swept-Wing Flow, NASA TM 108650

[2] T. I. Saeed, J. F. Morrison and M. S. Mughal, Roughness Effects on Swept-Wing Crossflow Transition in Moderate Free-Stream Turbulence, 29th Congress of the International Council

[3] N. Shahriari, M. R. Kollert, and A. Hanifi, Passive control of a swept-wing boundary layer using ring-type plasma actuators, Draft to be submitted.

[4] E. B. White, and W. S. Saric, Secondary instability of crossflow vortices, J. Fluid Mech. (2005), vol. 525, pp. 275–308.

[5] S. G. Saddoughi, and S. V. Veeravalli, Hot-wire anemometry behaviour at very high frequencies, Meas. Sci. Technol. 7 (1996) 1297–1300.